Available online at www.sciencedirect.com
SCIENCE DIRECT®
International Journal of Heat and Mass Transfer 48 (2005) 1999–2012
International Journal of HEAT and MASS TRANSFER
www.elsevier.com/locate/ijhmt

Heat transfer model of semi-transparent ceramics undergoing laser-assisted machining

Frank E. Pfefferkorn [a,*], Frank P. Incropera [b], Yung C. Shin [c]

[a] Department of Mechanical Engineering, University of Wisconsin-Madison, 1513 University Avenue, Madison, WI 53706, USA
[b] College of Engineering, University of Notre Dame, Notre Dame, IN 46556, USA
[c] School of Mechanical Engineering, Purdue University, West Lafayette, IN 47907-2088, USA

Received 27 April 2004; received in revised form 15 September 2004
Available online 4 March 2005

Abstract

A three-dimensional, unsteady heat transfer model has been developed for predicting the temperature field in partially-stabilized zirconia (PSZ) undergoing laser-assisted machining. The semi-transparent PSZ is treated as optically thick within a spectral band from approximately 0.5 to 8 μm. After comparing the diffusion approximation and the discrete ordinates method for predicting internal radiative transfer, suitability of the diffusion approximation is established from a comparison of model predictions with surface temperature measurements. The temperature predictions are in good agreement with measured values during machining. Parametric calculations reveal that laser power and feedrate have the greatest effect on machining temperatures.

1. Introduction

Laser-assisted machining (LAM) provides a means of increasing the material removal rate, improving dimensional control, and reducing surface flaws when shaping difficult-to-machine materials such as structural ceramics. A laser is used to locally heat the workpiece above a threshold temperature, reducing its yield strength below the fracture strength and enabling quasi-plastic material removal by a cutting tool, rather than brittle fracture. To characterize the process and to enhance understanding of related fundamentals, several experimental and theoretical studies have been performed. In particular, for opaque materials (silicon nitride and mullite) a transient three-dimensional thermal model of the process has been developed and experimentally validated [1], parametric effects have been considered [2], and the efficacy of the process for ceramics has been experimentally demonstrated [3–5]. However, unlike previous work, this study focuses on LAM of partially-stabilized zirconia (PSZ), which is semi-transparent [6] and hence able to volumetrically absorb, scatter, and emit radiation. Partially-stabilized zirconia is widely used as a structural ceramic, and its thermal conductivity is almost an order of magnitude smaller than that of silicon nitride.

This paper describes a transient, three-dimensional, heat transfer model of a semi-transparent PSZ workpiece undergoing LAM. Use of the diffusion approximation to determine internal radiative transfer is assessed by comparing predictions with those based on the more rigorous discrete ordinates method (DOM). The

* Corresponding author. Tel.: +1 608 263 2668; fax: +1 608 265 2316.
E-mail address: pfefferk@engr.wisc.edu (F.E. Pfefferkorn).

0017-9310/$ - see front matter © 2005 Elsevier Ltd. All rights reserved.
doi:10.1016/j.ijheatmasstransfer.2004.10.035

Nomenclature

c_p	specific heat, J/kg K
D_ℓ	laser beam diameter, mm
D_n	jet nozzle diameter, mm
d	depth-of-cut, mm
d_e	effective penetration depth, μm
E	emissive power, W/m^2
f	feed, mm/rev
f_r	feedrate, mm/min
H	characteristic length of radiation travel, m
H_n	nozzle-surface spacing, mm
h	enthalpy, J/kg
I	radiation intensity, W/m^2 sr μm
I_b	black-body radiation intensity, W/m^2 sr μm
k	phonon conductivity, W/m K; extinction coefficient (imaginary part of n_c)
k_{eff}	effective thermal conductivity, W/m K
k_r	radiation conductivity, W/m K
L_f	tool feed per revolution, mm
L_ℓ	laser-tool lead, mm
N	spindle speed, rpm
n	refractive index (real part of n_c)
n_c	complex index of refraction
P_ℓ	laser power, W
q''_{conv}	convective heat flux, W/m^2
q''_ℓ	incident laser flux, W/m^2
q'''_r	net radiation absorbed in a control volume, W/m^3
R_a	average surface roughness, μm
Re_j	jet Reynold's number
$\mathbf{r}$	position vector
r, ϕ, z	cylindrical coordinates directions
r_t	tool nose radius, mm
r_w	workpiece radius, mm
S	source term, W/m^3
T	temperature, K
t	time, s
t_p	preheat time, s
V_z	axial velocity, m/s
w_j	quadrature weight for discrete ordinate j
z_{ch}	axial location of the chamfer, m
z_{cv}	axial location of the chucked end of the workpiece, m
z_{fe}	axial location of the free end of the workpiece, m

Greek symbols

α_ℓ	laser absorptivity
β	$[\equiv\kappa + \sigma_s]$ extinction coefficient, m^{-1}
β_R	Rosseland-mean extinction coefficient, m^{-1}
Δr	radial control volume dimension, m
δT	sensitivity of temperature, °C
ε	emissivity
ϕ	azimuth angle, radians
ϕ_{flank}	circumferential extent of the flank wear region, rad
ϕ_ℓ	laser center–vertical angle, °
ϕ_p	laser center–pyrometer target angle, °
ϕ_t	laser center–tool angle, °
κ	absorption coefficient, m^{-1}
λ	wavelength, μm
μ, η, ξ	direction cosines defining discrete ordinate direction
Θ	cylindrical coordinate when deriving DOM, rad
ρ	density, kg/m^3
ρ_e	effective density, kg/m^3
ρ_λ	spectral reflectivity
σ	Stefan–Boltzmann constant, 5.67×10^{-8} W/m^2 K^4
σ_s	scattering coefficient, m^{-1}
τ_λ	optical thickness
Ω_ℓ	tool lead angle, °
$\mathbf{\Omega}$	unit direction vector
$\mathbf{\Omega}'$	unit direction vector of incident beam
ω	rotation rate, s^{-1}

Subscripts

b	black body
i	incident
mr	material removal
n	normal
pyro	pyrometer
sur	surroundings
λ	spectral

Superscripts

d	diffuse
s	specular

sensitivity to uncertainties in model parameters is determined, and predictions based on the complete model are compared with measured surface temperatures. A parametric study is performed to demonstrate the effect of the most influential operating parameters (laser power, feedrate, and depth-of-cut) on the workpiece temperature distribution.

The workpiece geometry and machining conditions for laser-assisted turning of a cylindrical workpiece, at some intermediate stage of machining, are shown in Fig. 1. Relative to the incident laser radiation and the cutting tool, motion of the workpiece is characterized by rotation and translation in the circumferential and axial directions, respectively. The boundary between

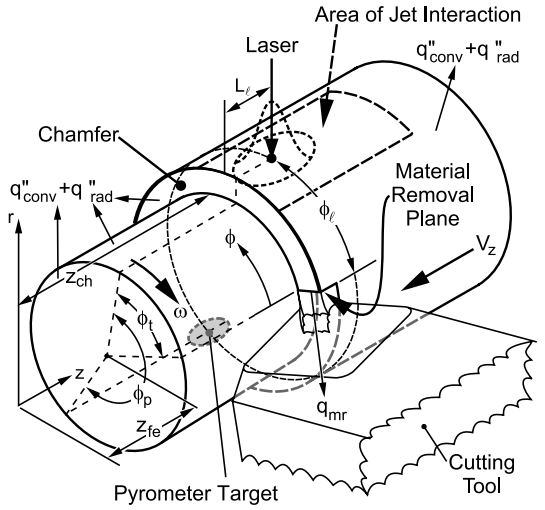

Fig. 1. Geometry of laser-assisted machining (after preheat: $t > t_p$).

machined and unmachined portions of the workpiece is represented by a helical chamfer, whose shape is defined by the cutting tool geometry and feedrate, and on which the small r–z plane at $\phi = 0$ corresponds to the location of material removal. The location of material removal relative to the laser center is designated by the parameters ϕ_ℓ and L_ℓ, where L_ℓ extends to the farthest edge of the chamfer. To facilitate a numerical solution of the temperature field, the material removal plane is approximated as a rectangle of depth d and width L_f, which corresponds to a cutting tool of zero lead angle ($\Omega_\ell = 0$) and radius ($r_t = 0$). The necessity of reaching a threshold temperature at the depth-of-cut for successful LAM requires a preheat phase during which the workpiece rotates with laser heating, but without machining or axial translation. During preheating the cylindrical workpiece does not have the helical chamfer or machined portion shown in Fig. 1, and the free end of the workpiece is located at the chamfer ($z_{fe} = z_{ch}$).

2. Experimental methods

Numerical simulation of the LAM process was coordinated with experiments conducted using a 1.5 kW (continuous wave) CO_2 laser, whose beam delivery is integrated with a CNC lathe [7], thereby synchronizing axial translation of the optics with that of the cutting tool. A radiation pyrometer [8] is mounted beneath the workpiece and moves with the laser beam and cutting tool in the axial (z) direction, thereby measuring the surface temperature at a fixed distance from the cutting zone and the laser-impingement location. The angles between the pyrometer target and laser center, $\phi_p = 212°$, the laser center and tool, $\phi_t = 55°$, and the laser center and vertical, $\phi_L = 10°$, are fixed (Fig. 1). The laser center leads the cutting tool in the axial direction ($L_\ell = 1.6$ mm), allowing time for energy to penetrate radially before material is removed by the cutting tool.

The pyrometer is a "single wavelength" sensor that measures radiation between 11 and 14 μm in order to avoid the CO_2 laser wavelength (10.6 μm) and to operate in a spectral range where PSZ is opaque ($\lambda > 8$ μm). The pyrometer can measure temperatures from 500 to 1500 °C, collecting 93% of the detected energy from a 2 mm diameter target at a focal distance of 162 mm. The total uncertainty associated with LAM measurements ranges from −33/+22 °C at a surface temperature of 500 °C to −59/+49 °C at 1000 °C [8]. Data are recorded at 1 kHz by a PC-based data acquisition system, and measured temperatures are based on the arithmetic average of five hundred data points.

Nominal experimental operating conditions correspond to a laser power, $P_\ell = 200$ W, a beam diameter, $D_\ell = 4.0$ mm, a laser-tool lead, $L_\ell = 1.6$ mm, a depth-of-cut, $d = 0.5$ mm, a feed rate, $f = 16$ mm/min, a spindle speed, $N = 800$ rpm, and a preheat time, $t_p = 6$ s. A compressed air jet ($Re_j = 20{,}000$, $D_n = 1.5$ mm, and $H_n = 21$ mm) is concentric with the laser beam and exits the laser nozzle to protect the optics. The PSZ workpieces are 15.00 mm in diameter by 63.75 mm long.

The LAM experiments are performed with fully-dense, sintered zirconia workpieces, which exhibit strong absorption above a wavelength of 5 μm, where optical properties are represented by the complex index of refraction, $n_{c,\lambda} = n_\lambda - ik_\lambda$ [6]. Scattering (at grain boundaries, inclusions, or pores) is significant for $\lambda < 5$ μm, but vanishes for $\lambda > 7$ μm, as the size of the scattering centers decreases relative to λ. Hence, absorption of radiation for $\lambda > 7$ μm depends more on material composition and crystal structure than on physical characteristics such as grain size, porosity, and glassy phase content, which vary significantly with the manner in which the ceramic is processed.

Results by Makino et al. [6], Tsukuma [9], and Wahiduzzaman and Morel [10] suggest that, while variations in chemical composition and processing can significantly affect the radiative properties of zirconia in the visible and near-infrared spectrums, all of the materials become opaque above a wavelength of $\lambda \approx 8$ μm [8]. Accordingly, the index of refraction, n_λ, and the extinction coefficient, k_λ, measured by Makino et al. [6] for $\lambda > 8$ μm are assumed to apply to the PSZ of this study. Although optical properties determined by Makino et al. are also used for $\lambda < 8$ μm, uncertainties are associated with the inability to assess the effect of differences between the materials used in this study and by Makino et al. However, the sensitivity of model predictions to such uncertainties is considered.

The PSZ used in this study is milky white in color, has an effective density of $\rho_e = 5770$ kg/m^3, and contains 4 mol% MgO. The samples have a monoclinic phase content of 4.2 mol%, with the remainder comprised of tetragonal and cubic phases [11], and a closed porosity of approximately 4.4% [8]. The grain size is approximately 50 μm with little grain boundary phase and an abundance of pores, which is typical of commercially available PSZ ceramics stabilized with MgO [12,13].

3. Mathematical model

Since zirconia ceramics are semi-transparent between wavelengths of 0.5 and 8.0 μm and opaque above 8 μm [6], internal heat transfer by radiation, as well as by diffusion and advection, must be included in the model. Advection is due to workpiece rotation and axial translation (V_z) in an Eulerian reference frame. Two different treatments of internal radiation are described.

3.1. Energy equation

The three-dimensional, transient temperature distribution, in cylindrical coordinates, may be determined from an energy equation of the form

$$\rho\left(\frac{\partial h}{\partial t}+\omega\frac{\partial h}{\partial \phi}+V_z\frac{\partial h}{\partial z}\right) = \frac{1}{r}\frac{\partial}{\partial r}\left(rk_{\text{eff}}\frac{\partial T}{\partial r}\right)+\frac{1}{r^2}\frac{\partial}{\partial \phi}\left(k_{\text{eff}}\frac{\partial T}{\partial \phi}\right)+\frac{\partial}{\partial z}\left(k_{\text{eff}}\frac{\partial T}{\partial z}\right)+S \tag{1}$$

where the first three terms on the left-hand side represent energy storage and circumferential and axial advection, respectively. The workpiece is always rotating at a rate, ω, whereas $V_z = 0$ during the preheat phase ($t \leqslant t_p$). The first three terms on the right-hand side represent energy diffusion in the radial, circumferential, and axial directions, respectively. These terms may include the effect of radiative transfer through an effective thermal conductivity, k_{eff}, if the diffusion approximation for radiation transfer is applicable. The last quantity in Eq. (1) is a source term accounting for internal generation, which may be due to a net volumetric rate of absorption of internal radiation or plastic deformation in the primary shear zone. However, relative to energy deposited by the laser, heat generation due to plastic deformation in the primary shear zone, as well as plastic deformation and friction in the secondary shear zone, have a negligible effect on the workpiece temperature distribution [1,2] and were therefore not included in the current model.

The temperature-dependent effective thermal conductivity, k_{eff}, and specific heat of PSZ were determined from specific heat and thermal diffusivity measurements made by TPRL, Inc. [14]. Effective thermal conductivity is represented by the following polynomial, where T is in degrees Kelvin,

$$k_{\text{eff}} = 1.17928\times10^{-9}T^3 - 2.45321\times10^{-6}T^2 + 5.19756\times10^{-4}T + 2.87954 \tag{2}$$

The thermal or phonon conductivity was empirically determined by fitting a second-order polynomial to data below 1000 °C,

$$k = \begin{cases} 1.99238\times10^{-7}T^2 - 1.27111\times10^{-3}T + 3.23083 & T \leqslant 1273\ \text{K} \\ 1.9356 & T > 1273\ \text{K} \end{cases} \tag{3}$$

The density of the PSZ was measured by the Archimedes method and found to be 5770 kg/m^3 at room temperature. This value was held constant in the model. The specific heat data are represented by the following polynomial,

$$c_p = \begin{cases} -1.1318\times10^{-4}T^2 + 0.34234T + 392.28 & T \leqslant 1450\ \text{K} \\ 650.71 & T > 1450\ \text{K} \end{cases} \tag{4}$$

3.2. Radiation transfer equation

For an absorbing, isotropically scattering, and emitting medium in local thermodynamic equilibrium with a uniform refractive index, the spectral radiation transfer equation can be written as [15]

$$\boldsymbol{\Omega}\cdot\nabla I_\lambda(\mathbf{r},\boldsymbol{\Omega}) = \kappa_\lambda(\mathbf{r})I_{b,\lambda}(\mathbf{r},\boldsymbol{\Omega}) - \beta_\lambda(\mathbf{r})I_\lambda(\mathbf{r},\boldsymbol{\Omega}) + \frac{\sigma_{s,\lambda}(\mathbf{r})}{4\pi}\int_{4\pi} I_\lambda(\mathbf{r},\boldsymbol{\Omega}')\,\mathrm{d}\boldsymbol{\Omega}' \tag{5}$$

Eq. (5) represents the change in spectral intensity of a beam traveling in the direction $\boldsymbol{\Omega}$ through a differential volume located at $\mathbf{r}$. Terms on the right-hand side represent, respectively, energy emitted into the direction $\boldsymbol{\Omega}$, attenuation of radiation by absorption and out-scattering, where $\beta_\lambda = \kappa_\lambda + \sigma_{s,\lambda}$, and energy scattered into the $\boldsymbol{\Omega}$ direction from radiation traveling through the volume in all other directions $\boldsymbol{\Omega}'$. Eq. (5) assumes isotropic scattering of unpolarized light in a medium is at local thermodynamic equilibrium.

The spectral index of refraction, n_λ, absorption coefficient, κ_λ, and scattering coefficient, $\sigma_{s,\lambda}$, have been determined for dense PSZ in the spectral region from 0.5 μm to 8 μm [6]. The refractive index is approximately constant ($n \approx 2$) in this band, while the absorption and scattering coefficients, which vary significantly with wavelength, are represented by the following polynomials.

$$\sigma_{s,\lambda} = \begin{cases} 79.248\lambda^3 - 273.68\lambda^2 + 286.45\lambda - 63.256 \\ \quad 0.5 \leqslant \lambda \leqslant 1.4\ \mu\text{m} \\ 0.0022407\lambda^6 - 0.074731\lambda^5 + 1.029\lambda^4 \\ -7.5288\lambda^3 + 31.241\lambda^2 - 71.486\lambda + 74.821 \\ \quad 1.4 < \lambda \leqslant 8.0\ \mu\text{m} \end{cases} \tag{6}$$

$$\kappa_\lambda = 4.0112 \times 10^{-5}\lambda^6 - 8.1845 \times 10^{-4}\lambda^5 + 6.6624 \times 10^{-3}\lambda^4 - 0.026335\lambda^3 + 0.051768\lambda^2 - 0.045802\lambda + 0.023741 \quad 0.5 \leqslant \lambda \leqslant 8.0\ \mu\text{m} \tag{7}$$

The scattering and absorption coefficients determined by Makino et al. [6] are independent of temperature over the measured range from 290 to 700 K.

3.3. Boundary conditions

3.3.1. Radiative effects

Partially-stabilized zirconia (PSZ) can be treated as opaque to laser radiation at 10.6 μm (CO_2 laser), since the effective penetration depth ($d_e \approx 24$ μm) is less than the radial dimension of the surface control volumes used in the numerical simulation [7]. Hence, the normal spectral absorptivity for laser radiation can be equated to the normal spectral emissivity at $\lambda = 10.6$ μm at which, $\alpha_\ell = \varepsilon_{n,\lambda} \approx 0.95$ [8,16]. The validity of this assumption was tested by radially dividing the top control volume of the numerical mesh ($\Delta r = 50$ μm) into three sub volumes ($\Delta r = 16.7$ μm) and using Beer's law with the spectral absorption coefficient of PSZ ($\kappa_\lambda = 42.32\ \text{mm}^{-1}$ at $\lambda = 10.6$ μm) [6] to estimate the amount of energy absorbed in each sub volume [7]. Although the corresponding maximum surface temperature beneath the laser can be as much as 250 °C less than predictions based on assuming that all of the laser energy is absorbed in the larger ($\Delta r = 50$ μm) control volume, differences in the predictions of the material removal temperature, T_{mr}, and the temperature at the pyrometer measurement location, T_{pyro}, are less than a 20°.

For radiation emitted within the workpiece, the interface between the workpiece and the surroundings represents a boundary that transmits and reflects internal radiation. Accordingly, the radial boundary condition for the radiation transfer equation may be expressed as

$$I_\lambda(\boldsymbol{\Omega}) = \frac{\rho_\lambda^d}{\pi} \int_{\hat{\mathbf{n}}\cdot\boldsymbol{\Omega}'<0} I_\lambda(\boldsymbol{\Omega}')|\hat{\mathbf{n}}\cdot\boldsymbol{\Omega}'|\mathrm{d}\Omega' + \rho_\lambda^s I_\lambda(\boldsymbol{\Omega}_s) \tag{8}$$

The first term on the right-hand-side represents the diffuse component of reflected energy propagating from the interface in the direction $\boldsymbol{\Omega}$, and the second term represents the specularly reflected component, where $\boldsymbol{\Omega}_s$ is the direction from which radiation must hit the surface in order to travel into the direction of $\boldsymbol{\Omega}$ after a specular reflection [17]. However, since data on the internal reflectivity of structural zirconia are nonexistent, it is assumed that the unmachined surface (ground) is a specular reflector, and the boundary condition becomes

$$I_\lambda(\boldsymbol{\Omega}) = \rho_\lambda^s I_\lambda(\boldsymbol{\Omega}_s) \tag{9}$$

Fresnel's and Snell's laws are used to determine the relation between the magnitudes and directions of the incident and reflected radiation at the assumed optically smooth interface. The discrete specular reflectivity used in Eq. (9) is defined to preserve the reflected radiative flux in the direction normal to the surface [18]. The surfaces of the DOM grid that are located within the FVM grid (Fig. 2) are treated as transparent to radiation. The complexity of treating the DOM in the ϕ-direction due to stepwise discretization of the chamfer is avoided by locating the z-direction boundary of the DOM grid adjacent to the chamfer.

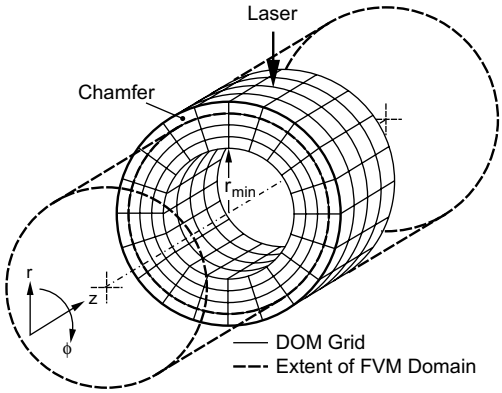

Fig. 2. Schematic of grid used to solve radiative transfer equation.

3.3.2. Energy equation

Since the workpiece surface experiences convection, emitted radiation, and absorbed laser radiation (Fig. 1), the radial boundary condition for the unmachined portion of the surface corresponds to

$$k\left.\frac{\partial T}{\partial r}\right|_{r=r_w} = \alpha_\ell q''_\ell(\phi,z) - q''_{conv}(\phi,z) - E(T) \tag{10}$$

Radiation emission from the surface of the workpiece is expressed as

$$E(T) = \varepsilon\sigma T^4 \tag{11}$$

when the diffusion approximation to radiative transfer is applied, and as

$$E(T) = \int_{8\ \mu\text{m}}^{\infty} \varepsilon_\lambda(\lambda,T)\pi I_{b,\lambda}(\lambda,T)\mathrm{d}\lambda \tag{12}$$

when internal radiation is modeled by the discrete ordinates method. The diffusion approximation assumes that

all of the radiation emitted by one control volume is absorbed and scattered in its neighboring control volumes. With this model the surface layer of control volumes may be treated as opaque over all wavelengths. The discrete ordinates method determines the radiation intensity distribution for the semi-transparent waveband (0.5–8.0 μm) and inherently accounts for energy which exits the workpiece within this wavelength interval. Therefore, emission from the surface is restricted to the opaque waveband above 8.0 μm. Expressing the spectral hemispherical emissivity as $\varepsilon_\lambda = \alpha_\lambda = 1 - \rho_\lambda$ and obtaining the spectral distribution of the hemispherical reflectivity, ρ_λ, from Makino et al. [6], the total hemispherical emissivity may be evaluated from the expression

$$\varepsilon(T) = \frac{\int_0^\infty \varepsilon_\lambda(\lambda) E_{\lambda,\mathrm{b}}(\lambda, T)\mathrm{d}\lambda}{E_\mathrm{b}(T)} \tag{13}$$

The corresponding value of ε varies from 0.67 at 300 K to 0.37 at 2100 K, and a nominal value of 0.5 is used in the numerical simulations. A sensitivity analysis (Section 5.1) showed that, the model is least sensitive to the total emissivity, but very sensitive to laser absorptivity, for which a constant value is used due to a lack of temperature dependent data for α_ℓ. The lack of data for contrasting as-sintered and smooth surfaces requires use of the same emissivity and absorptivity for all surface conditions.

The spatial distribution of the laser irradiation, $q''_\ell(\phi, z)$, is Gaussian [7]. The heat flux $q''_{\mathrm{conv}}(\phi, z)$ is associated with forced convection due to a gas jet which impinges on the workpiece and protects the focusing optic from machining debris [7], or with mixed convection from portions of the workpiece outside the jet interaction zone (Fig. 1). Eq. (10) is also applied to the machined surface ($r_{\mathrm{w,m}} = r_\mathrm{w} - d$), which may be overlapped by the laser spot, depending on prescribed values of the laser beam diameter D_ℓ and laser-tool lead L_ℓ.

On the chamfer, the energy balance is of the form

$$k\left.\frac{\partial T}{\partial z}\right|_{z=z_{\mathrm{ch}(\phi)}} = q''_{\mathrm{conv}} + E(T) \tag{14}$$

for $r_{\mathrm{w,m}} \leqslant r \leqslant r_\mathrm{w}$ and $0 \leqslant \phi \leqslant 2\pi - \phi_{\mathrm{flank}}$. The region between ϕ_{flank} and 2π represents the contact area between the tool flank and the workpiece (the tertiary zone). Since energy generation due to frictional heating between the tool and workpiece has a negligible effect on the material removal and pyrometer temperatures [1,2], the corresponding boundary conditions may be approximated as

$$k\left.\frac{\partial T}{\partial z}\right|_{z=z_{\mathrm{ch}(\phi)}} = 0 \tag{15}$$

At the machined and chucked ends of the workpiece, respectively,

$$k\left.\frac{\partial T}{\partial z}\right|_{\substack{z=z_{\mathrm{ch}}(t\leqslant t_\mathrm{p}) \\ z=z_{\mathrm{fe}}(t>t_\mathrm{p})}} = q''_{\mathrm{conv}} + E(T) \tag{16}$$

$$\left.\frac{\partial T}{\partial z}\right|_{z=z_{\mathrm{cv}}} = 0 \tag{17}$$

where the small thermal diffusivity of partially-stabilized zirconia ($\sim 1 \times 10^{-6}\ \mathrm{m^2/s}$) permits treatment of the chucked end as an adiabatic boundary. At all locations away from the material removal plane, circumferential continuity of temperatures and temperature gradients yields boundary conditions of the form

$$T(r, \phi, z) = T(r, \phi + 2\pi, z) \tag{18}$$

$$\left.\frac{\partial T}{\partial \phi}\right|_{\phi} = \left.\frac{\partial T}{\partial \phi}\right|_{\phi+2\pi} \tag{19}$$

At the initiation of laser heating, the workpiece is in thermal equilibrium with the surroundings.

$$T(r, \phi, z, t = 0) = T_{\mathrm{sur}} \tag{20}$$

At the material removal plane, energy is advected out of the system with the chips. This region corresponds to $\phi = 0$ and includes an area bounded by $r = r_\mathrm{w}$, $r = (r_\mathrm{w} - d)$, $z = z_{\mathrm{ch}}$, and $z = (z_{\mathrm{ch}} + L_\mathrm{f})$. The corresponding boundary condition can be represented by the surface energy balance

$$-\frac{k_{\mathrm{eff}}}{r}\left.\frac{\partial T}{\partial \phi}\right|_{\phi=0} = \rho c_p r \omega (T - T_{\mathrm{ref}}) \tag{21}$$

which equates energy lost by advection from the computational domain to energy transfer by conduction to the removal plane.

4. Numerical method

4.1. Diffusion approximation

The diffusion approximation to radiative transfer in an optically thick medium is based on Rosseland's simplification of the radiative transfer equation [17], for which the radiative flux,

$$\mathbf{q}''_\mathrm{r} = -k_\mathrm{r} \nabla T \tag{22}$$

is proportional to a radiation conductivity that is a function of temperature cubed. Since the effect of radiation is embodied in the effective thermal conductivity, k_{eff}, only the energy equation must be solved. The approximation applies to an optically thick medium for which the product of the extinction coefficient, β_λ, and a characteristic dimension H of the medium is much greater than one ($\tau_\lambda \equiv \beta_\lambda H \gg 1$). Defining H as the smallest radial length

of the finite-volume grid ($H = 0.0625$ mm), values of τ_λ over that portion of the spectrum ($0.5\ \mu m < \lambda < 8\ \mu m$) for which spectral absorption and scattering coefficients are published [6] vary from $\tau_\lambda \approx 1.5$ at $\lambda = 0.5\ \mu m$ to $\tau_\lambda \approx 0.1$ at $\lambda = 8\ \mu m$, neither of which satisfies the requirement that $\tau_\lambda \gg 1$. If H is approximated by a representative depth-of-cut for LAM ($d \sim 1$ mm), the optical thickness would vary from $\tau_\lambda \approx 24$ at $\lambda = 0.5\ \mu m$ to $\tau_\lambda \approx 1.6$ at $\lambda = 8\ \mu m$. Hence, conditions cannot be characterized as optically thick and a more rigorous procedure for predicting the internal radiation field, such as the discrete ordinates method (DOM), may be needed.

When the diffusion approximation is invoked, numerical solution of the energy equation is facilitated by using the following formulation of Eq. (1) [19],

$$\begin{aligned}\rho\left(\frac{\partial(c_pT)}{\partial t}+\omega\frac{\partial(c_pT)}{\partial\phi}+V_z\frac{\partial(c_pT)}{\partial z}\right)&=\frac{1}{r}\frac{\partial}{\partial r}\left(rk_{\text{eff}}\frac{\partial T}{\partial r}\right)+\frac{1}{r^2}\frac{\partial}{\partial\phi}\left(k_{\text{eff}}\frac{\partial T}{\partial\phi}\right)\\&+\frac{\partial}{\partial z}\left(k_{\text{eff}}\frac{\partial T}{\partial z}\right)+S+\rho\frac{\partial}{\partial t}\left(c_pT^*-h^*\right)\\&+\rho\omega\frac{\partial}{\partial\phi}\left(c_pT^*-h^*\right)+\rho V_z\frac{\partial}{\partial z}\left(c_pT^*-h^*\right)\end{aligned}\tag{23}$$

The last three terms on the right-hand-side are added source terms, where T^* and h^* are the values of T and h at the current iteration. When equilibrium is reached the c_pT terms on both sides cancel and Eq. (23) reverts to Eq. (1).

4.2. Coupled radiation/diffusion

The discrete ordinates method (DOM) is based on transforming the integro-differential equation (Eq. (5)) into a set of simultaneous partial differential equations. Solutions are obtained for a set of n different directions $\mathbf{\Omega}_i$, and the integrals over direction are replaced by numerical quadratures [20,21].

The divergence of the radiation intensity in cylindrical coordinates may be written as [22,23]

$$\mathbf{\Omega}\cdot\nabla I=\frac{\mu}{r}\frac{\partial(rI)}{\partial r}+\frac{\eta}{r}\frac{\partial I}{\partial\Theta}+\xi\frac{\partial I}{\partial z}-\frac{1}{r}\frac{\partial(\eta I)}{\partial\phi}\tag{24}$$

where μ, η, and ξ are direction cosines representing the fraction of radiation intensity projected into the directions of the unit vectors $(\mathbf{e}_r, \mathbf{e}_\Theta, \mathbf{e}_z)$, such that $\mathbf{\Omega} = \mu\mathbf{e}_r + \eta\mathbf{e}_\Theta + \xi\mathbf{e}_z$. Discretizing Eq. (5) and combining with Eq. (24) allows the radiative transport equation for cylindrical coordinates to be represented as

$$\begin{aligned}\frac{\mu}{r}\frac{\partial(rI_\lambda)}{\partial r}+\frac{\eta}{r}\frac{\partial I_\lambda}{\partial\Theta}+\xi\frac{\partial I_\lambda}{\partial z}-\frac{1}{r}\frac{\partial(\eta I_\lambda)}{\partial\phi}&\\=\kappa_\lambda I_{b,\lambda}-\beta_\lambda I_\lambda+\frac{\sigma_{s,\lambda}}{4\pi}\sum_{j=1}^{n}w_jI_\lambda(\mathbf{\Omega}_j)&\end{aligned}\tag{25}$$

The S4-approximation [23] is used to solve Eq. (25) simultaneously with the energy equation (Eq. (1)) for each of twenty-four ordinate directions. The two equations are coupled through dependence of the radiation field on temperature and dependence of temperature on the net volumetric rate of radiation absorption. The net rate of radiation absorbed in a control volume, q'''_r, is a required input to the source term in the energy equation.

$$\begin{aligned}q'''_r&=\kappa_\lambda(\mathbf{r})\left[\int_{4\pi}I_\lambda(\Omega)-4\pi I_{b,\lambda}\right]\\&\cong\kappa_\lambda(\mathbf{r})\left[\sum_{j=1}^{n}w_jI_\lambda(\Omega_j)-4\pi I_{b,\lambda}\right]\end{aligned}\tag{26}$$

Therefore, when solving for internal radiation with the DOM, it is necessary to iterate between the solvers for the energy equation and the radiation transport equation. The gray-body assumption is used to model the spectral behavior of PSZ in the semi-transparent waveband ($0.5 < \lambda < 8\ \mu m$), and the radiative properties are averaged over this spectral range.

4.3. Computational domain

The computational domain is divided into a set of nonoverlapping control volumes, and the finite-volume method (FVM) is used to discretize the energy equation [24]. The discretized equations are formulated in a fully implicit scheme. After each iterative solution of the resulting algebraic equations the new temperature field is used to update the temperature-dependent variables and to calculate the radiation intensity distribution if radiation is determined by the DOM.

The energy equation is solved in a nonuniform, structured grid of $50\times40\times170$ (ϕ, r, z) control volumes for which grid independence was determined by doubling the number of circumferential control volumes without any change in predicted temperatures. Convergence of the solution is achieved if the residual is less than 10^{-6}, resulting in a global energy balance of less than 10^{-3} W and an average change of less than 0.01% in specific heat between iterations.

The computational domain for the DOM subroutine is divided into a set of nonoverlapping control volumes (Fig. 2), and for computational expediency it is coarser than the FVM grid. The DOM grid is comprised of $15\times18\times33$ (ϕ, r, z) control volumes whose surfaces coincide with the control surfaces of the FVM grid. The extent of the DOM grid is iteratively determined by placing its boundaries such that, at these extremities, the radiation flux is negligible compared with the diffusion flux. The exception is the boundary which coincides with the machining interface. Here the magnitude of the radiation flux is comparable to diffusion, however, the

DOM grid is not extended beyond the machining interface in order to keep the problem manageable.

Because the DOM is solved on a coarser grid, the temperature used by the DOM subroutine to determine the black body intensity is a volume-weighted average of the temperatures predicted by solving the energy equation. The finite-volume method is used to spatially discretize Eq. (25), and angular discretization follows the discrete ordinates method [23,25–27]. The direct differencing method introduced by Carlson and Lathrop [25] is used to discretize the angular derivative in Eq. (25). The step scheme is used to express the variation of the radiation intensity across the control volume because it does not generate unrealistic negative intensities [20]. After each iteration of the resulting algebraic equations the new radiation field is used to determine the net rate of radiation absorption, q_r''', which is part of the source term, S, in the energy equation (Eq. (23)).

Fig. 3 shows the predicted surface temperature distribution as well as the near-surface r–z plane temperature distributions at the cutting plane and laser center. These results demonstrate that large temperature gradients exist in all three coordinate directions, hence a three-dimensional model is required.

4.4. Comparison of predictions for the radiation models

Since PSZ does not meet the requirement of being optically thick, the effect of invoking the diffusion approximation is assessed by comparing temperatures determined by the diffusion approximation with those obtained by using the discrete ordinates method (DOM). The comparison is made for the nominal operating conditions of Table 1.

Fig. 4 compares surface temperature measurements with those predicted at the same location using the diffusion approximation and the discrete ordinates method. Sensitivity (uncertainty) in the solutions, as indicated by the bars, is a result of uncertainties in parameters required by the model. The shorter run-time for the DOM solution (17.7 s) is due to the larger computational requirements but is sufficient for the comparison.

Although the shapes of the predicted temperature histories are similar, results of the discrete ordinates method are approximately 130 °C less than those predicted by the diffusion approximation, and the measured temperature approaches a quasi-steady state that is intermediate to the predictions. Both models overpredict the measurements during the preheat and early machining stages ($t < 10$ s). Results of the DOM simulations are in better agreement with the measurements for $t < 20$ s, but at $t = 40$ s the measured surface temperature is approximately equidistant from the diffusion and extrapolated DOM predictions.

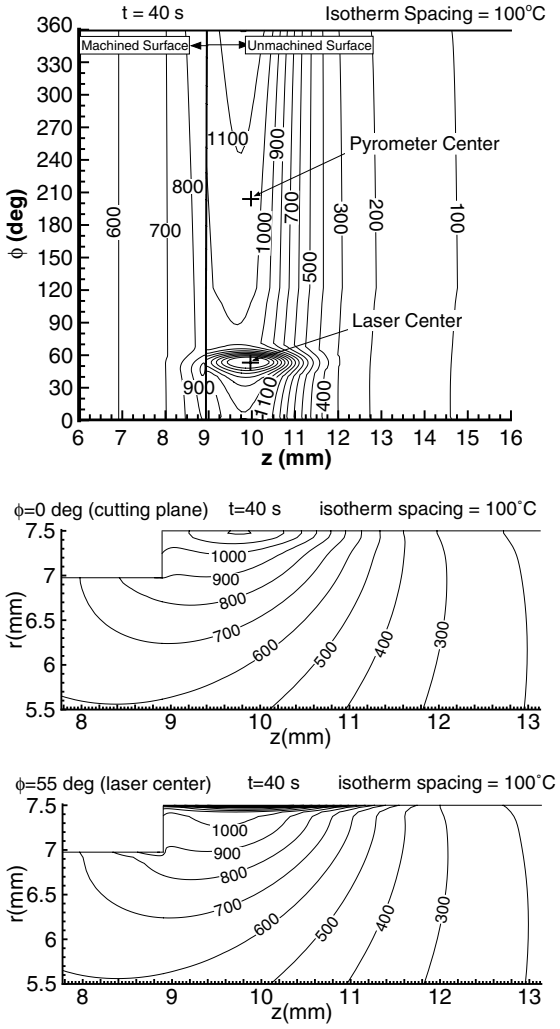

Fig. 3. Predicted temperature fields (°C) based on the diffusion approximation, $t = 40$ s, nominal conditions: machined and unmachined surface, r–z plane at the cutting plane ($\phi = 0°$), and r–z plane beneath the laser center ($\phi = 55°$).

Table 1
Nominal operating conditions

Parameter	Magnitude
P_ℓ	200 W
D_ℓ	4.0 mm
L_ℓ	1.6 mm
d	0.5 mm
f (f_r)	0.02 mm/rev (16 mm/min)
N	800 rpm
t_p	6 s

Predictions based on the DOM are well below those of the diffusion approximation at both the location of the temperature measurement (Fig. 4) and across the

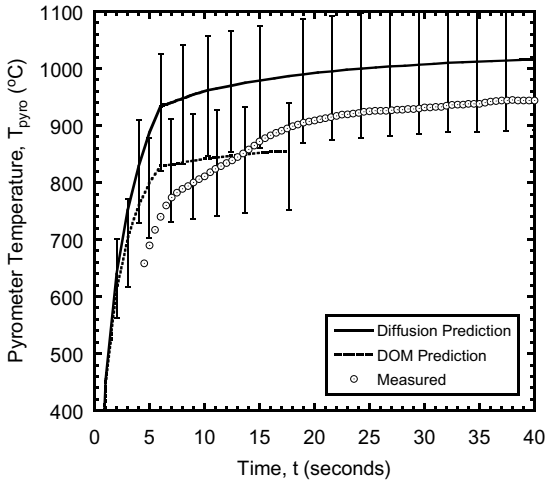

Fig. 4. Comparison of measured and predicted temperatures at the pyrometer measurement location for the two radiation models.

material removal plane. Similarly, Figs. 5 and 6, which provide axial temperature fields at $t = 17.7$ s for circumferential locations corresponding to the laser center and material removal plane, respectively, reveal significantly lower temperatures throughout the workpiece for the DOM simulation. Since the absorption of laser radiation is equivalent for the two simulations, it follows that the

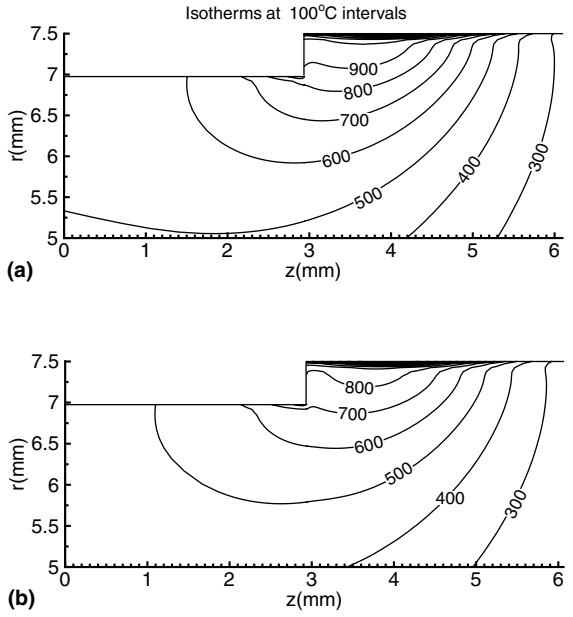

Fig. 5. Comparison of predicted temperature fields (°C) based on the diffusion approximation and DOM: r–z plane beneath the laser center, $t = 17.7$ s, nominal conditions. (a) Diffusion approximation and (b) DOM solution.

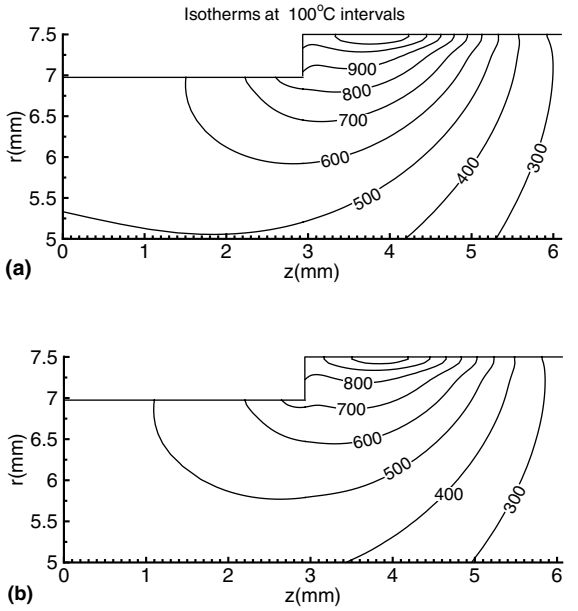

Fig. 6. Comparison of predicted temperature fields (°C) based on the diffusion approximation and DOM: r–z plane at material removal location, $t = 17.7$ s, nominal conditions. (a) Diffusion approximation and (b) DOM solution.

DOM model provides for more radiation of this energy to the surroundings from the chamfer. This result is attributed to the transparent boundary condition assumed for the surface coinciding with the chamfer. However, at the chamfer, some of the incident radiation from the workpiece is actually reflected back into the workpiece, thereby causing underprediction of the temperature field by the DOM method. If internal reflectivity data were available and could be applied to the chamfer surfaces, temperatures predicted by the DOM would exceed those of Figs. 5 and 6, and would perhaps approach those of the diffusion approximation. The steep temperature gradients near the surface of the workpiece, immediately beneath the laser, are due to treatment of the laser irradiation as a surface phenomenon. The optically smooth assumption for the circumferential interface results in a significant amount of radiation being reflected inward and not transmitted to the surroundings. Therefore, in the immediate vicinity of the laser, energy is not lost as readily as at the chamfer and the local temperatures predicted by the diffusion approximation and the DOM are in closer agreement than at the material removal plane.

Although the DOM model predicts lower temperatures at the measurement location than the diffusion approximation, the sensitivity limits of both models encompass the measured temperature during the machining phase ($t > 6$ s). Moreover, there is a great deal of uncertainty in the radiative properties and

boundary conditions used in the DOM model, which is not considered in the sensitivity analysis. Since the more rigorous solution of internal radiation with the DOM does not provide more insight or benefit to the goal of accurately predicting the material removal temperature, the remainder of this study will focus on temperature predictions made by the diffusion approximation.

5. Results and discussion

5.1. Sensitivity/uncertainty

The sensitivity of model predictions to parameter uncertainties was determined by varying a single parameter in each of several simulations for the nominal conditions (Table 1). The absorptivity to laser radiation, α_ℓ, jet impingement heat transfer coefficient, h, specific heat, c_p, effective thermal conductivity, k_{eff}, and total emissivity, ε, were varied according to the uncertainties given in Table 2.

Uncertainties in the jet impingement heat transfer coefficient relate to its magnitude and spatial distribution. Since the correlation for impingement of a submerged jet on a flat plate is being applied to the cylindrical workpiece, uncertainties in the spatial variation of the heat transfer coefficient cannot be determined and only the magnitude is varied [7]. The temperature-dependent specific heat and thermal conductivity were measured for the PSZ of this study [14], and the estimated ±10% uncertainty is attributed to the effects of LAM on creation of a heat-affected zone with a high crack density and associated property variations. Since the spectral emissivity used to calculate is taken from the literature [28], significant uncertainty may be associated with the varying surface conditions of this study.

Sensitivity is defined as the difference between numerical predictions based on the nominal value and the uncertainty limits of Table 2. The sensitivity of the predicted temperature, δT_x, to each variable, x, is determined as a function of temperature. The total sensitivity, δT, of the material removal, T_{mr}, and pyrometer, T_{pyro}, temperatures is determined from the following quadrature, $\delta T = \sqrt{\delta T_\alpha^2 + \delta T_h^2 + \delta T_k^2 + \delta T_{\text{cp}}^2 + \delta T_\varepsilon^2}$. Because they directly influence the amount of deposited energy, the absorptivity and convective heat transfer coefficient have the greatest effect on the model predictions. While some constituent sensitivities display a nonlinear temperature dependence, the total sensitivity of the pyrometer temperature, T_{pyro}, varies nearly linearly with temperature from +40/−55 °C at 400 °C to +140/−165 °C at 1400 °C. Similarly, the sensitivity of the material removal temperature, δT_{mr}, varies nearly linearly from +30/−40 °C at 400 °C to +140/−165 °C at 1400 °C.

Table 2
Uncertainty in model parameters

Parameter	Nominal value	Uncertainty (value range)
Laser absorptivity, α_ℓ	0.95	+5/−10% (1.0–0.85)
Jet impingement heat transfer coefficient, h	[7]	±20%
Specific heat, c_p	Eq. (4)	±10%
Effective thermal conductivity, k_{eff}	Eq. (2)	±10%
Total emissivity, ε	0.5	±40% (0.7–0.3)

5.2. Model validation

Surface temperature measurements made at a location axially aligned with and 212° downstream from the laser center (Fig. 1) are used to assess the heat transfer model. The sensitivity of the predicted temperature at the measurement location to model parameters is similar to that of the material removal temperature, and a comparison of predicted and measured values of T_{pyro} is therefore adequate for assessing the ability of the model to predict the material removal temperature, T_{mr}. Previous investigations for mullite and silicon nitride [1,3–5] have established that the laser power, feed, and depth-of-cut have the greatest impact on the temperature field and hence the LAM process. Therefore, three feedrates (f_r = 8, 16, and 32 mm/min), four laser powers (P_ℓ = 150, 200, 250, and 300 W), and three depths-of-cut (d = 0.5, 0.75, and 1.0 mm) are considered adequate for assessing the accuracy of the model.

Fig. 7 compares the measured and predicted temperature histories as a function of laser power, P_ℓ. In all

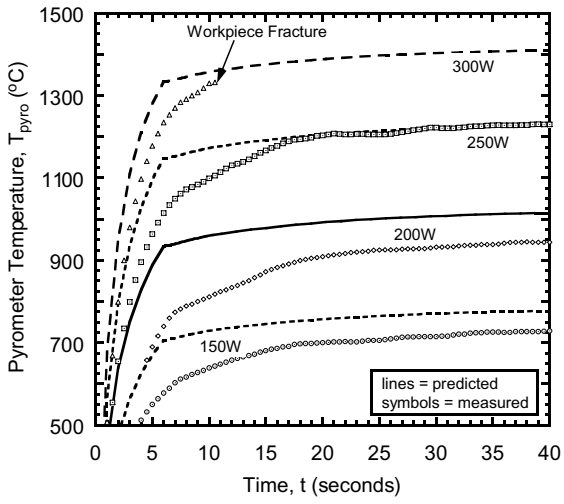

Fig. 7. Effect of laser power on the temperature history at the pyrometer location.

four cases there is greater discrepancy between predictions and measurements during preheat ($t < 6$ s) than later in the process, when temperatures change more slowly with time and quasi-steady conditions are reached. The agreement between temperatures is significantly better for the 250 and 300 W conditions. The model sensitivity is significantly larger than the measurement uncertainty, and except during preheat, the measured temperature is within the sensitivity limits. Therefore, disparities between the data and the model are only associated with the preheat condition. At 300 W the measured temperature rapidly approaches the predicted temperature, until the workpiece fractures and no more data are collected.

The feedrate controls the amount of energy deposited per unit length of traversed material and hence has a significant impact on the temperature field. Fig. 8 compares predicted and measured temperatures for different feedrates. The measured values show excellent repeatability during preheat but are much lower than the predicted temperatures. However, differences between measured and predicted values decrease with increasing time and temperature. After 6 s preheat, the high feedrate reduces energy deposition per unit length of the workpiece and requires less time to traverse the 10 mm distance of the cut. This reduction lowers the temperature below that achieved at the end of preheating. The slowest feedrate is half as fast as the nominal condition and deposits more energy per unit distance, resulting in higher temperatures and better agreement between measured and predicted values under quasi-steady conditions, as is the case at higher laser powers.

The model indicates that the surface temperature at the measurement location is relatively insensitive to variations in the depth-of-cut, d. The measured temperatures are almost identical for $d = 0.5$ mm (nominal) and $d = 0.75$ mm, but increase by approximately 65 °C for the quasi-steady state of $d = 1.0$ mm. An increase in near chamfer temperatures with increased depth-of-cut was also found for silicon nitride [29] and is attributed to a greater resistance to heat flow around a deeper chamfer. However, for the measurement location, it is not known why there is very little variation between $d = 0.5$ and 0.75 mm and a sudden increase at $d = 1.0$ mm.

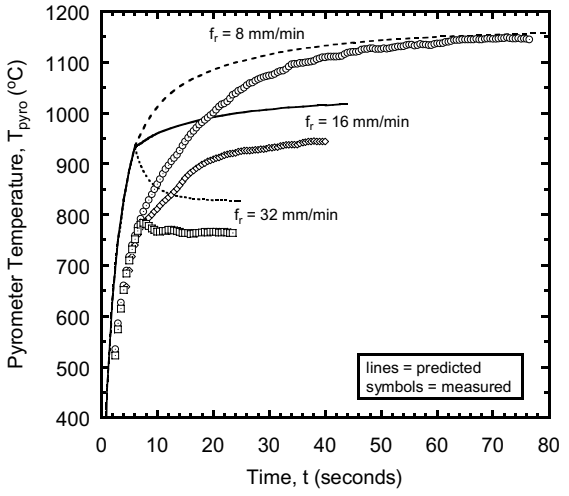

Fig. 8. Effect of feedrate on the temperature history at the pyrometer location.

The discrepancy between measured and predicted temperatures during preheat is attributed to uncertainty in the spectral emissivity for the pyrometer waveband (11–14 μm). The surface temperature measurement is very sensitive to uncertainty in emissivity [8], and if the value at room temperature is lower than indicated in the literature [28] and increases with heating and the creation of the heat-affected zone (HAZ) [7,30], measured temperatures would be initially lower than actual values. The measurement uses a fixed emissivity, $\varepsilon = 0.97$, which may approximate the true value of a PSZ surface characterized by a high crack density in the HAZ associated with quasi-steady conditions.

The sensitivity of the heat transfer model to relevant parameters and the uncertainty in the temperature measurements are large and need refinement. Within these limits the predicted temperatures provide reasonable agreement with the measured values during the later stages of the LAM process but do not do so during preheating. The model does a good job of predicting trends due to changes in the laser power and feedrate. The temperature of interest in evaluating LAM of PSZ is the material removal temperature, which cannot be measured, but can be predicted. In all cases, the pyrometric surface temperature measurement is in good agreement with predictions for $35 < t < 40$ s, which is the time over which temperatures and forces are averaged for machinability analysis. Therefore, it can be said that, for matters concerning machinability, the heat transfer model accurately predicts the surface temperature, T_{pyro}, and the material removal temperature, T_{mr}, with acceptable accuracy.

5.3. Parametric study

The effects of laser power, P_ℓ, feedrate, f_r, depth-of-cut, d, spindle speed, N, laser diameter, D_ℓ, and preheat time, t_p, on the material removal temperature, T_{mr}, were studied. Fig. 9 shows the monotonic, almost linear variation of T_{mr} with P_ℓ. Laser power is the primary means of controlling the temperature, and since the sensitivities of T_{pyro} and T_{mr} to P_ℓ are similar, the effect of laser power on T_{mr} can be detected at the pyrometer measurement location and corrected with the use of a feedback controller.

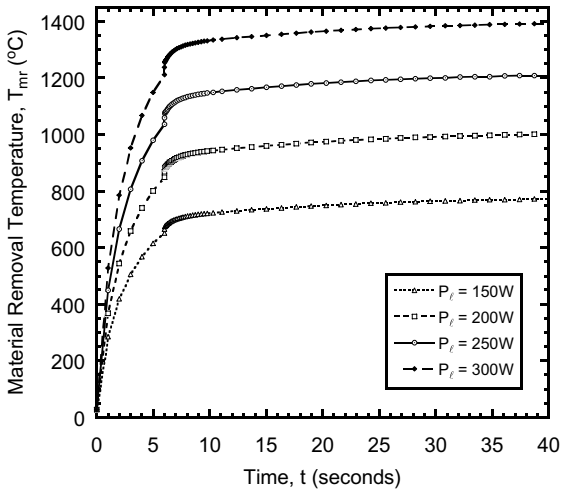

Fig. 9. Variation of material removal temperature with laser power.

The effect of feedrate was studied by varying the feed while keeping all other machining parameters constant, including the spindle speed ($N = 800$ rpm). As shown in Fig. 10, the preheat phase is identical in all three cases, but when machining begins, the amount of energy deposited per unit length varies according to the feedrate. The higher feed results in less energy being deposited per unit length. Therefore, while an increase in the feedrate is desirable to increase productivity, it must be accompanied by another measure to increase the local energy input in order to maintain a sufficiently large value of T_{mr}. Under quasi-steady conditions at the end of the 10 mm cut, $T_{mr} = 830$, 1020, and 1150 °C and $T_{pyro} = 850$, 1000, 1110 °C for $f_r = 32$, 16, and 8 mm/min, respectively, showing a similar dependence on feedrate.

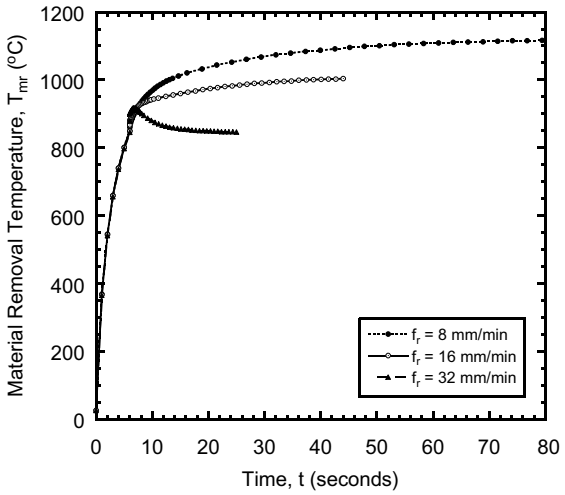

Fig. 10. Variation of material removal temperature with feedrate.

Understanding the effect of depth-of cut, d, is important to increasing productivity and being able to design a process for creating contoured parts. The predicted pyrometer temperature and the maximum surface temperature are relatively insensitive to changes in d. However, depth-of-cut has a significant effect on the average, T_{mr}, and the minimum, $T_{mr,min}$, material removal temperatures. Increasing d from 0.5 to 1.0 mm results in a decrease from 1000 to 950 °C and 930 to 800 °C for T_{mr} and $T_{mr,min}$, respectively. The average material removal temperature, T_{mr}, is believed to be the best metric for evaluating the efficacy of LAM. However, the minimum material removal temperature, $T_{mr,min}$, may determine operating conditions for which the workpiece has not been softened enough, resulting in excessive wear or breakage of the tool tip. Therefore, the greater sensitivity of $T_{mr,min}$ to d is significant, due to the inability of temperature measurements at the current pyrometer location to detect the effect of changes in d. For future temperature control during LAM, a measurement location which is also sensitive to changes in d must be found (possibly on the chamfer itself).

Axial temperature fields (r–z plane) coinciding with the material removal plane for $d = 0.5$ and 1.0 are shown in Fig. 11. The increased resistance to heat transfer around the larger depth-of-cut is most clearly seen by the change in the 600 °C isotherm at $z \sim 8$ mm. The lower left hand corner of Fig. 11(b) has a lower temper-

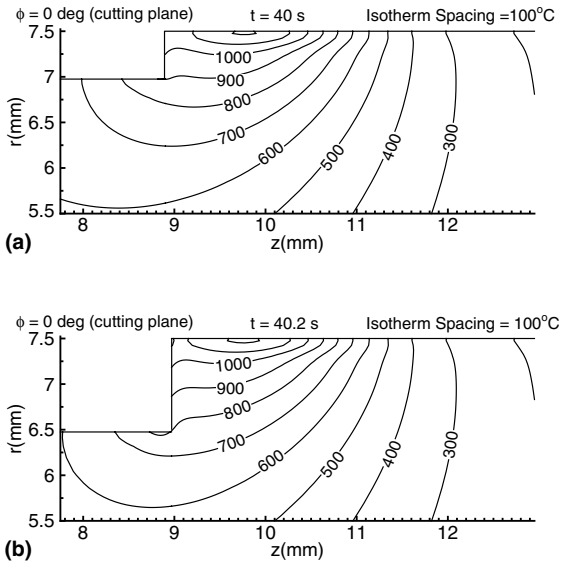

Fig. 11. Effect of depth-of-cut on temperature in r–z plane coincident with material removal location ($t \sim 40$ s). (a) 0.5 mm depth-of-cut and (b) 1 mm depth-of-cut.

ature than the equivalent region in Fig. 11(a) as a result of less energy penetrating to this location. Hence, more energy is trapped in the near-chamfer region for $d = 1.0$ mm, resulting in higher temperatures in that part of the material removal plane corresponding to $d = 0.5$ mm.

The laser beam diameter, D_ℓ, was varied to control the incident laser flux and limit the scope of heating. A small beam diameter results in higher laser fluxes and higher maximum surface temperatures, T_{max}, which can induce local melting and microstructural changes. It also provides a larger driving potential for energy diffusion radially inward. If the pyrometer remains axially aligned with the laser center and 212° downstream, T_{pyro} increases 110 °C from 1020 to 1130 °C as D_ℓ decreases from 4 to 3 mm, compared with a 210 °C increase in T_{mr}. The benefit of decreasing the laser diameter is in the increased material removal temperature for the same amount of deposited energy.

The effect of rotational speed was studied by varying the spindle speed, N, while keeping the feedrate constant so that the same amount of energy is deposited per unit distance. Energy is more rapidly advected away from the laser impingement location at higher N, reducing the energy which is stored locally and hence reducing T_{max}. Conversely, energy that is advected to the pyrometer measurement location increases T_{pyro}. The effects of variations in N are greater near the surface of the workpiece than at the depth-of-cut and result in a relatively small change in T_{mr}, which decreases with increasing N due to energy being more efficiently distributed to locations away from the material removal plane.

The preheat time is used to bring the temperature of the workpiece to a level that enables cutting at the initiation of tool contact. If this temperature is not achieved, the results can be tool failure, workpiece failure, accelerated tool wear, unacceptable surface finish, and/or surface damage. Increasing the preheat time increases the amount of energy deposited in the workpiece and thereby the temperature. In order to generate a uniform temperature during LAM, it is necessary to match the preheat time with the operating conditions so that, ideally, the steady-state temperature is achieved at the end of preheat. The present thermal model can be used to determine a suitable preheating cycle.

6. Conclusions

A transient, three-dimensional heat transfer model is developed, and temperature predictions based on an optically thick assumption (diffusion approximation) for internal radiative transfer are compared with those based on a discrete ordinates method of solution (DOM). Measured surface temperatures are found to lie within the sensitivity limits of both predictions. During the machining phase it is found that the diffusion approximation and the DOM solution overpredict and underpredict measured temperatures, respectively. The discrepancy between the measured and predicted surface temperatures during preheating (both models) is attributed to an initial overprediction of the surface emissivity, which then increases with temperature and crack development in the heat-affected zone. The diffusion approximation is selected for use in subsequent predictions on the basis of computational convenience and satisfactory agreement with measured temperatures.

A sensitivity analysis of parameter uncertainties on temperature predictions shows that laser absorptivity and convective heat transfer coefficient have the greatest effect on the predictions. Cumulative uncertainties in the pyrometer measurement and material removal temperatures vary almost linearly from +40/−55 °C at 400 °C to +140/−165 °C at 1400 °C and from +30/−40 °C at 400 °C to +140/−165 °C at 1400 °C, respectively. Because temperatures at the measurement and material removal locations show approximately the same sensitivity to parameter uncertainties, it is assumed that the predictions of T_{mr} are also accurate within current measurement and predictive capabilities.

Within the measurement and model uncertainties, the temperature predictions are in good agreement with measured values during machining ($t > t_p$), and the model is successful in predicting trends due to changes in the laser power and feedrate. However, it predicts a negligible effect of the depth-of-cut in contrast to measured temperatures, which increase with depth-of-cut. The level of agreement between predictions and measurements increases with temperature, and the laser power and feedrate have the greatest effect on the material removal temperature. Since similar effects characterize the pyrometer temperature, it can be used with confidence to exercise control of LAM.

Acknowledgement

Support of this work by the National Science Foundation under grant nos. 9802047-CTS and 0115172-DMI and the School of Mechanical Engineering at Purdue University through the Laura Winkelman and Ingersoll-Rand fellowships is gratefully acknowledged.

References

[1] J.C. Rozzi, F.E. Pfefferkorn, F.P. Incropera, Y.C. Shin, Transient, three-dimensional heat transfer model for the laser assisted machining of silicon nitride: I. Comparison of predictions with measured surface temperature histories, Int. J. Heat Mass Transfer 43 (2000) 1409–1424.

[2] J.C. Rozzi, F.P. Incropera, Y.C. Shin, Transient, three-dimensional heat transfer model for the laser assisted

machining of silicon nitride: II. Assessment of parametric effects, Int. J. Heat Mass Transfer 43 (2000) 1425–1437.
[3] S. Lei, Y.C. Shin, F.P. Incropera, Experimental investigation of thermo-mechanical characteristics in laser assisted machining of silicon nitride ceramics, ASME J. Manufact. Sci. Eng. 123 (2001) 639–646.
[4] P.A. Rebro, Y.C. Shin, F.P. Incropera, Laser-assisted machining of reaction sintered mullite ceramics, ASME J. Manufact. Sci. Eng. 124 (4) (2002) 875–885.
[5] J.C. Rozzi, F.E. Pfefferkorn, Y.C. Shin, F.P. Incropera, Experimental evaluation of the laser assisted machining of silicon nitride ceramics, ASME J. Manufact. Sci. Eng. 122 (4) (2000) 666–670.
[6] T. Makino, T. Kunitomo, I. Sakai, H. Kinoshita, Thermal radiation properties of ceramic materials, Heat Transfer—Japanese Res. 13 (4) (1984) 33–50.
[7] F.E. Pfefferkorn, Laser-assisted machining of zirconia ceramics, Ph.D. thesis, Purdue University, West Lafayette, IN, 2002.
[8] F.E. Pfefferkorn, F.P. Incropera, Y.C. Shin, Surface temperature measurement of semi-transparent ceramics by long-wavelength pyrometry, ASME J. Heat Transfer 125 (1) (2002) 48–56.
[9] K. Tsukuma, Transparent titania–yttria–zirconia ceramics, J. Mater. Sci. Lett. 5 (1986) 1143–1144.
[10] S. Wahiduzzaman, T. Morel, Modeling of the effect of translucence of engineering ceramics on heat transfer in diesel engines, ASME Paper 89-HT-1, 1989.
[11] K.J. Bowman, F.E. Pfefferkorn, Y.C. Shin, Recrystallization textures during laser-assisted machining of zirconia ceramics, Mater. Sci. Forum 408–412 (2002) 1669–1674.
[12] O.C. Standard, C.C. Sorell, Densification of zirconia—conventional methods, Key Eng. Mater. 153-154 (1998) 251–300.
[13] R. Chaim, A.H. Heuer, V. Aronov, Surface microstructure changes on laser treatment of MGO-partially-stabilized zirconia, J. Am. Ceram. Soc. 73 (6) (1990) 1519–1523.
[14] R.E. Taylor, H. Groot, J. Ferrier, Thermophysical properties of TBC, TPRL 2438, TPRL, Inc., West Lafayette, IN, 2000.
[15] M.N. Özisik, Radiative Transfer and Interactions with Conduction and Convection, Wiley, New York, 1973.
[16] Y.S. Touloukian, Thermophysical Properties of High Temperature Solid Materials, The Macmillan Company, New York, 1967.
[17] R. Siegel, J.R. Howell, Thermal Radiation Heat Transfer, third ed., McGraw-Hill, New York, 1992.
[18] M. Song, R. Viskanta, Discrete ordinates solution of axisymmetric radiative transfer within a condensed semi-transparent medium having specularly reflecting boundaries, in: Proceedings of 31st National Heat Transfer Conference, HTD-vol. 325/3, ASME, 1996, pp. 55–62.
[19] J.Y. Murthy, S.R. Mathur, A conservative numerical scheme for the energy equation, ASME J. Heat Transfer 120 (1998) 1081–1086.
[20] J.C. Chai, S.V. Patankar, H.S. Lee, Evaluation of spatial differencing practices for the discrete-ordinates method, J. Thermophys. Heat Transfer 8 (1) (1994) 140–144.
[21] W.A. Fiveland, J.P. Jessee, Comparison of discrete ordinates formulations for radiative heat transfer in multidimensional geometries, J. Thermophy. Heat Transfer 9 (1) (1995) 47–54.
[22] G.C. Pomraning, The Equations of Radiation Hydrodynamics, Pergamon Press, Oxford, 1973.
[23] E.E. Lewis, J.W.F. Miller, Computational Methods of Neutron Transport, Wiley, New York, 1984.
[24] S.V. Patankar, Numerical Heat Transfer and Fluid Flow, Taylor & Francis, London, 1980.
[25] B.G. Carlson, K.D. Lathrop, Transport theory—the method of discrete ordinates, in: K. Greenspan, C.N. Kelber, D. Okrent (Eds.), Computing Methods in Reactor Physics, Gordon and Breach Science Publishers, New York, 1968.
[26] K.D. Lathrop, Use of discrete-ordinates methods for solution of photon transport problems, Nucl. Sci. Eng. 24 (1966) 381–388.
[27] W.A. Rhoades, R.L. Childs, An Updated Version of the DOT 4 One- and Two-Dimensional Neutron/Photon Transport Code, ORNL-5851, Oak Ridge National Laboratory, Oak Ridge, TN, 1982.
[28] Y.S. Touloukian, D.P. DeWitt, Thermal Radiative Properties of Nonmetallic Solids, Plenum Publishing, New York, 1972.
[29] J.C. Rozzi, Experimental and theoretical evaluation of the laser assisted machining of ceramic materials, Ph.D. thesis, Purdue University, West Lafayette, IN, 1997.
[30] F.E. Pfefferkorn, Y.C. Shin, F.P. Incropera, Y. Tian, Laser-assisted machining of magnesia-partially-stabilized zirconia, ASME J. Manufact. Sci. Eng. 126 (1) (2004) 42–51.